Journal of Applied Polymer Science

WILEY

Applied Polymer SCIENCE

RESEARCH ARTICLE OPEN ACCESS

Combined Foaming and Surface Structuring of Polymers With Supercritical Carbon Dioxide ($scCO_2$) Applying an Incomplete Saturation Strategy

Luisa Maren Borgmann[1] | Ester Priante[1] | Siegbert Johnsen[2] | Marc Schneider[1] | Markus Guttmann[1] | Benedikt Bläsi[3] | Gabriele Wiegand[2] | Hendrik Hölscher[1]

[1]Institute of Microstructure Technology (IMT) at the Karlsruhe Institute of Technology (KIT), Karlsruhe, Germany | [2]Institute of Catalysis Research and Technology (IKFT), Karlsruhe Institute of Technology (KIT), Karlsruhe, Germany | [3]Fraunhofer Institute for Solar Energy Systems (ISE), Freiburg, Germany

Correspondence: Hendrik Hölscher (hendrik.hoelscher@kit.edu)

Received: 12 November 2025 | **Revised:** 16 January 2026 | **Accepted:** 16 January 2026

Keywords: applications | molding | nanostructured polymers | optical properties | structure-property relationships

ABSTRACT

Supercritical carbon dioxide ($scCO_2$) is a widely applied solvent utilized in many physical–chemical processes, including the foaming or structuring of polymers. Here, we demonstrate that the last two can be combined in one process step applying an incomplete saturation strategy, resulting in foamed and structured polymer sheets with multi-functionality. Caused by the nano- and micropores, the polymer sheets scatter light, leading to a white color impression. Due to the imprinted nano- and microstructures, the polymer surfaces feature an increased water contact angle and reduced optical reflection due to the moth-eye effect.

1 | Introduction

Supercritical CO_2 ($scCO_2$) is frequently applied in chemical engineering [1–4]. Foaming with $scCO_2$, for example, has been proven to be a suitable method to produce nanopores in polymer foils and particles [5–7]. If these pores effectively scatter light of all visible wavelengths, the foaming of the polymer results in its pigment-free white appearance, even though the unprocessed material might be transparent. Consequently, this process might be utilized for the whitening of surfaces, replacing TiO_2 particles as scatterers which are under critical discussion due to their energy-intensive production [8] as well as their potential harm to human health by nanometer-sized TiO_2 particles [9–11].

Additionally, (supercritical) CO_2 may also assist in the imprinting of nano- and microstructures in polymer surfaces [12–16]. Such CO_2 assisted embossing strategies employ that pressurized CO_2 plasticizes polymers with good CO_2 solubility [17]. Thus, the effective glass transition temperature T_g decreases strongly, and the polymer eventually becomes deformable even at room temperature [18, 19]. Consequently, embossing is possible at greatly reduced operation temperatures compared to conventional approaches like hot embossing or thermal nanoimprinting, where the polymer is heated close to or over its glass transition temperature T_g [20]. Therefore, CO_2 assisted embossing is a promising alternative, especially for the processing of thermally degradable polymers [12]. Furthermore, CO_2 assisted embossing leaves no traces of solvent behind in the polymer and, due to the easy separation of mold and sample, chemical release agents can be omitted [12].

Interestingly, foaming and structuring with $scCO_2$ have been considered as two independent processes so far. Foaming was even considered an unwanted effect during CO_2 assisted embossing, and actively prevented [13]. Here, we demonstrate that $scCO_2$ can be utilized for simultaneous foaming as well as nano- and micro-structuring, resulting in pigment-free white polymer sheets with functional surface structures.

2 | Experimental

2.1 | PMMA Sheets

The utilized sheets of poly(methyl methacrylate) (PMMA) (UPAG AG) had a nominal sheet thickness of 1 mm. To fit into our autoclave, the respective polymer sheets were trimmed to squares with a size of $15 \times 15\,mm^2$.

2.2 | Processing of Polymer Sheets With Supercritical Carbon Dioxide

To achieve $scCO_2$ assisted simultaneous imprinting and foaming of polymer sheets, we extended our previously applied batch process [5, 7]. For that, the polymer sample is placed into a home-built autoclave, displayed in Figure 1a, which is subsequently sealed. A syringe pump (ISCO D-Series) pressurizes the CO_2 and leads it into the autoclave. In this way, the polymer is exposed to CO_2 at constant temperature and pressure, which causes its T_g to decrease, that is, it gets plasticized [17]. In the next step, the pressure is rapidly released; thereby, the solubility of CO_2 in the polymer matrix decreases. Due to the new pressure and temperature conditions, the polymer becomes supersaturated, and nucleation occurs [1, 21, 22]. Consequently, pores start to grow as CO_2 diffuses out of the polymer matrix into nuclei of a critical size. Hereby, the glass temperature rises again, and the pore structure stabilizes as T_g reaches the temperature of the sample [1, 21, 22].

For the combination of the foaming process with imprinting of structures, we extended our setup with structured molds, that are pressed into a polymer surface during the foaming process with $scCO_2$. In previous studies, the mold was pressed into the polymer sample with the help of weights [12] or clamps [14]. Here, we utilized neodymium magnets (Type NdFeB N45, EarthMag GmbH, Germany) with two different nominal strengths (5 and 8 kg) to press the mold into the polymer surface [5]. In this way, the sample and mold are sandwiched between the magnets. As the thickness of the molds and the PMMA sheets are about 0.4 and 1 mm, respectively, the magnets are 1.4 mm apart. However, due to the direct contact of the PMMA sheet and the backside magnet, it simultaneously acts as diffusion barriers, limiting the diffusion of $scCO_2$ into the polymer sample. Therefore, to facilitate $scCO_2$ diffusion from the bottom of the polymer sheet, a metal wire mesh (mesh size = 0.5 mm) was placed between the sample and one magnet, as shown in Figure 1b.

As Wang et al. [12] reported that the imprinting of the mold into the polymer improves with increasing $scCO_2$ pressure, we applied the highest suitable pressure of our setup, which is 50 MPa. The exposure time was 30 min and the applied process temperatures were 40°C, 60°C, and 80°C. The latter value is the maximum operating temperature of the magnets, specified by the manufacturer, limiting our process temperature. With the applied process parameters above 10 MPa, we do not expect to be retrograde region reported in some studies on PMMA treated with $scCO_2$ [23–25].

2.3 | Molds

We used metallic molds in our study, as polymer molds might get plasticized by CO_2 and ceramic molds are not suitable for the fast temperature changes during pressure release. Two types of electroplated molds manufactured via interference lithography [26, 27] were utilized for the structuring of bio-inspired micro- and nanostructures, respectively.

A shim featuring micro-scaled structures to mimic the lotus effect was fabricated at the Fraunhofer Institute for Solar Energy Systems (ISE, Freiburg, Germany). Its microscale bumps have a squared arrangement and an average peak-to-peak distance of about 3.22 μm and an average depth of about 2.42 μm.

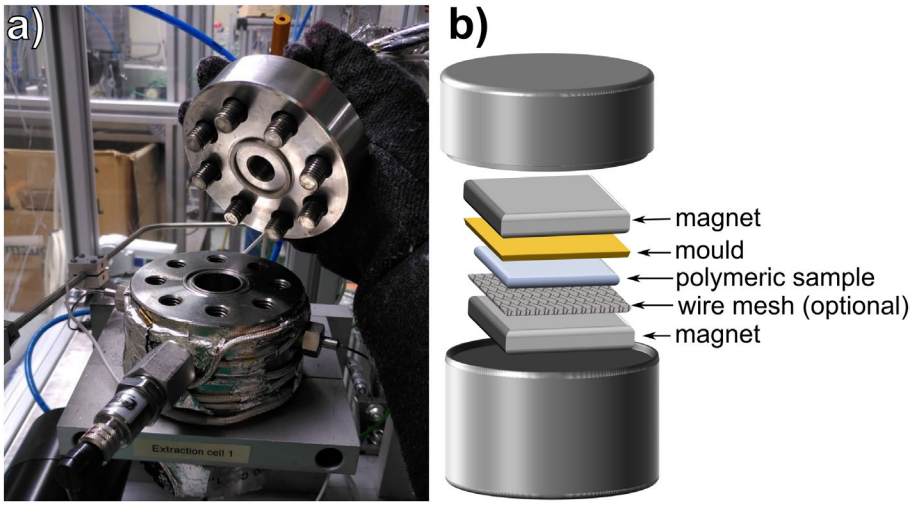

FIGURE 1 | (a) Photo of the autoclave. Its cylindrical cavity is 90 mm high and has a diameter of 27 mm. (b) Schematic sample arrangement utilized for foaming and simultaneous patterning of a polymer sheet with $scCO_2$ in a batch process. The gray open cylinders at top and bottom represent the opened autoclave shown in (a). To facilitate diffusion of $scCO_2$, a wire mesh can be placed between sample backside and magnet. Without it, the magnet and the mold insert act as diffusion barrier. The applied process temperatures in this study were between 40°C and 80°C with an applied pressure of 50 MPa. [Color figure can be viewed at wileyonlinelibrary.com]

A nanostructured nickel mold (Type HT-AR-02XS, temicon GmbH) with nanoscale nipples was used to replicate a moth's eye structure. The mold is designed to imprint polymers to reduce the reflectivity below 0.2%. It has a size of $25 \times 25\,mm^2$ and features a $20 \times 20\,mm^2$ large area of hexagonally arranged nanoscale nipples. The nominal average depth (vertical distance from peak to adjacent valley) is about 350 nm, and the nominal peak-to-peak distance is 290 nm. Since the original mold was too large for our autoclave chamber, we produced a smaller replica of it. For that, the original nanoscale pattern was first transferred into a sheet of PMMA by hot embossing [20] at a temperature of 155°C and with a force of 30 kN. This negative polymeric replica of the mold was metallized with Cr/Au using PVD processing and subsequently electroplated with nickel, resulting in a positive copy of the original mold. A standard nickel sulphamate electrolyte was used, and the current density was increased stepwise with 0.1, 0.25, 0.5 and 1.0 A/dm^2 applied for exposure times of 60, 66, 2, and 24 h, respectively. The final copy in nickel, separated from the PMMA replica by lift-off, had a size of about $1.5 \times 2.0\,cm^2$ and an average structure depth of about 310 nm.

2.4 | Analytical Methods

2.4.1 | Optical Microscopy

Surface and pore structures were inspected with an optical microscope (Axioscope 5/7/Vario, Zeiss GmbH, Germany). The open-source image processing package *Fiji* was used for the evaluation of the micrographs [28].

2.4.2 | Scanning Electron Microscopy

Scanning electron microscopy (SEM, Zeiss SUPRA 60 VP, Zeiss GmbH, Germany) was applied for the characterization of surfaces and pore structures. Non-metallic samples were sputtered with a thin layer of silver before imaging. Again, the image processing package *Fiji* was utilized for further analysis [28]. Based on the SEM micrographs, the cell density N_0 in different sections of the samples was calculated utilizing the approach of Li et al. [29]

$$N_0 = N_f / \left(1 - V_f\right) \tag{1}$$

here N_f is the number of pores per μm^3 of foamed polymer calculated by $N_f = (n/A)^{3/2}$ with n the number of pores in the area A [μm^2] occupied by pores. V_f is the volume occupied by the (spherical) pores per μm^3, which is estimated by

$$V_f = (\pi / 6)\, D^3\, N_f \tag{2}$$

where D is the average pore diameter.

2.5 | Atomic Force Microscopy

Surface height profiles of embossed polymer structures and the respective molds were examined by atomic force microscopy (AFM, Dimension Icon, Bruker AG, Germany). Rectangular silicon cantilevers (All-in-One, Budget Sensors) were used for imaging in dynamic mode (tapping-mode). The evaluation of the topography was conducted with the open-source software *Gwyddion* [30].

2.6 | Contact Angle Measurements

To determine the influence of the imprinted structures on the wettability of the polymeric surfaces, a commercial contact angle meter (Dataphysics OCA 40 micro) was used for static contact angle measurements. The automatic dispenser was set to a liquid volume of 1 µL with a dosing rate of 1 µL/s. The samples were rinsed with de-ionized water to remove possible dirt particles sticking to the surface and carefully dried with compressed air.

2.7 | Optical Spectroscopy

The optical properties of the samples were examined via reflectance measurements with a UV–Vis–NIR Spectrophotometer (Lambda 950, PerkinElmer) equipped with an integrating sphere. All measurements were normalized with a diffuse reflectance standard (Spectralon, Labsphere).

3 | Results and Discussion

3.1 | Incomplete Saturation Strategy

Our initial tests with the set-up shown in Figure 1 revealed that treatments with $scCO_2$ easily imprint the mold's structure into the polymer's surface. However, if the polymer sheet is allowed to saturate completely with $scCO_2$, we saw unwanted deformations of the structured surface. This observation agrees with previous studies reporting deformations caused by the imprint of gas voids for polymer particles foamed in a diffusion barrier [7, 31]. To avoid this unwanted effect, we applied an *incomplete* saturation strategy where the polymer is foamed and structured after an exposure time that is insufficient to completely saturate the polymer throughout the material's thickness. Consequently, the $scCO_2$ concentration is reduced towards the side covered with the mold and this side is not foamed, preventing unwanted deformations (see more detailed discussion below).

To achieve an incomplete $scCO_2$ uptake, we roughly estimated the exposure time in the following way. Based on the diffusion coefficients from literature for $scCO_2$ and PMMA at 38°C and 25 MPa, a PMMA sheet of 1 mm thickness has a saturation time between 25 and 260 min depending on the respective molecular weight [29]. As the last parameter was not exactly known in our case, we chose the shortest saturation time. Additionally, we considered an additional time span of 5 min to account for the prolonged saturation from one side. Thus, an exposure time of 30 min was applied in all experiments presented here. As sketched in Figure 1b, we considered two sample arrangements.

For hindered diffusion, sheet and mold were clamped directly between two magnets without a wire mesh. In this case, the

polymer sheets stayed transparent after the $scCO_2$ treatment at different temperatures, as shown in Figure 2. Only a white frame indicates foaming of the polymer caused by diffusion of $scCO_2$ from the edges. The noticeable extension of the foamed frame with increasing foaming temperature is due to the faster diffusion at higher temperatures [29, 32]. However, although the inner part of the PMMA sheets stayed transparent, an iridescent surface is observable with the naked eye. This optical effect already indicates the successful imprint of microstructures into the polymer surface, acting as a diffraction grating.

To facilitate diffusion, we placed a wire mesh at the bottom side of the polymeric sheets. Subsequently, we treated the stack of magnet, mold, polymer sheet, wire mesh, and magnet with $scCO_2$ applying the same conditions as for the hindered diffusion. Afterwards, the sheets appear completely white as the bottom side of the sheet is completely foamed. However, as intended by the incomplete saturation strategy, the corresponding cross-sections of these white samples reveal a transparent, unfoamed layer at the mold side (see Figure 2). Towards the wire mesh side, however, a white, foamed layer is created. Additionally, the structure of the wire mesh partly imprints into the foamed surface, too. The overall foamed layer thickness increases with process temperature. For the samples foamed at 40°C, 60°C and 80°C, it is about 400, 1000, and 1400 μm, respectively. This observation can be explained by the fact that the diffusion coefficient increases for higher foaming temperatures, thus $scCO_2$ diffuses deeper into the polymer [29, 32]. Additionally, the pore sizes are expected to increase with rising temperature [33]. This effect contributes further to the growth of the foamed layer. The optical micrographs of the cross-sections prove that the incomplete saturation strategy allows structuring and foaming of the polymer sheets as planned.

3.2 | Analysis of Pore Size and Density

Already, the optical microscopy analysis of samples' cross-sections presented in Figure 2 revealed that samples processed with facilitated diffusion feature a white, foamed side and a transparent, seemingly non-porous side. This observation is confirmed by SEM images, as shown in the cross-sectional overview in Figure 3. The side facing the mold is indeed non-porous. The wire mesh facing side, in contrast, is porous with microscale pores in a transition zone between unfoamed and porous divisions. However, as can be expected from the optical microscopy images shown in Figure 2, the porous layer extends deeper into the polymer sheets for increasing processing temperatures, as the diffusion rate of $scCO_2$ in polymers increases at higher temperatures [32]. The porous side shows a distinct size gradient, resulting in smaller pores close to the surface facing the mesh facilitating diffusion, while the pore size increases towards the transition zone. For samples foamed at 40°C, however, no transition zone is observed, and the pore diameters are smaller than 100 nm. The samples obtained at 60°C and 80°C process temperature have pore sizes in the order of a few hundred nanometers close to the mesh side but up to a few micrometers close to the transition zone. Macropores larger than 50 μm are not considered.

The observation of a gradient in pore size throughout the sample is in good agreement with previous studies [34–36]. As in our study, the pore size gradient reported by Zhou et al. [35] is due to incomplete saturation, but they induced the foaming by subsequent heating between hot plates. In the study of Ngo et al. [36] the formation of a gradient is caused by a temperature gradient in a specifically designed autoclave. Syurik et al. [34] combined both strategies with incomplete saturation and a temperature

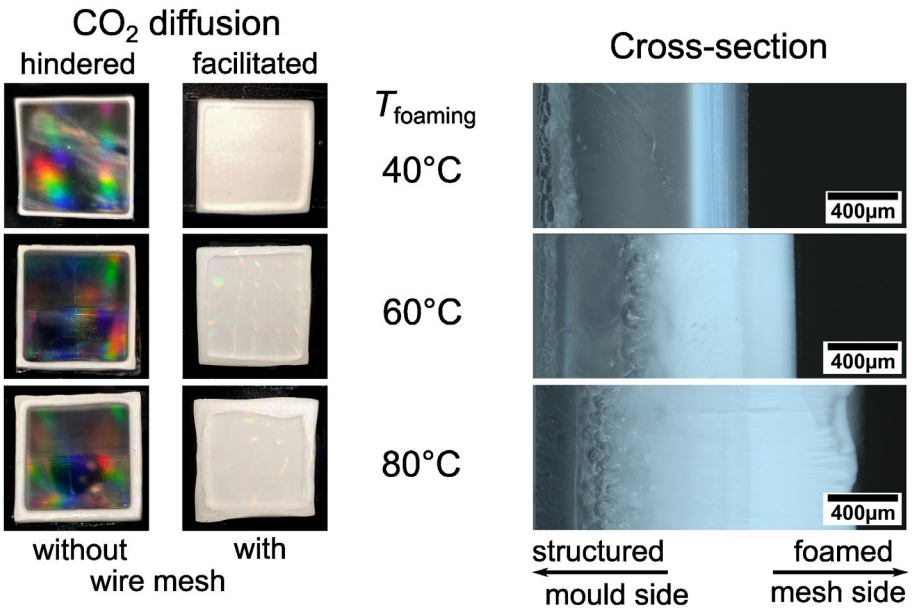

FIGURE 2 | Comparison of PMMA sheets (15×15 mm) foamed and microstructured at different temperatures, either without (hindered diffusion) or with a mesh (facilitated diffusion). The PMMA sheets treated with $scCO_2$ without a mesh stay transparent in the middle. The sheets processed with a mesh, on the other hand, appear white because the mesh allowed the diffusion of $scCO_2$ into the polymer sheets, resulting in foamed white polymer sheets. Nonetheless, both show colorful diffraction patterns caused by the imprinted surface structure. The optical micrographs at the right-side display the respective cross-sections of the white foamed and structured samples. The thickness of the respective white layer increases with foaming temperature. The structured side, nevertheless, is unfoamed. [Color figure can be viewed at wileyonlinelibrary.com]

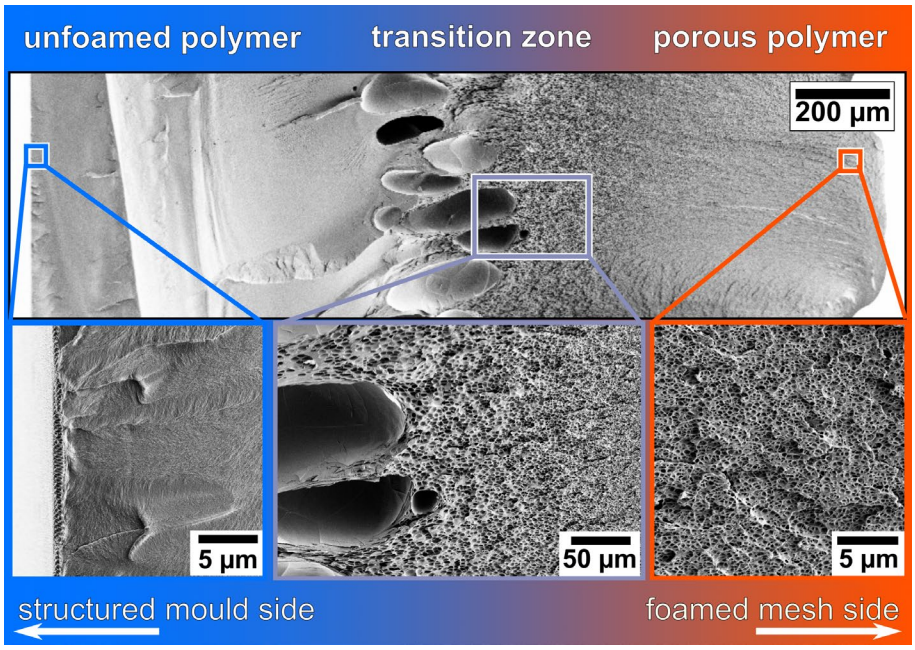

FIGURE 3 | SEM micrograph of the cross-section of a foamed polymer, which was exposed to $scCO_2$ diffusion from only one side (mesh side) resulting in a pore size gradient. The side facing the mold is non-porous with a structured surface. Between the non-porous and the porous side, a transition zone with some large macropores (longer than 50 µm) is formed. Pores closer to the mesh side are smaller than the ones closer to the transition zone. [Color figure can be viewed at wileyonlinelibrary.com]

gradient in an additional heating step. The pore size gradient achieved by incomplete saturation can be explained by the gradient in $scCO_2$ absorbed throughout the thickness of the polymer [35]. Due to short exposure times, a higher saturation is reached near the surface, through which CO_2 diffuses in, compared to regions located deeper in the polymer.

After the pressure quench, the polymer is supersaturated and the higher the supersaturation, the lower is the activation energy barrier for nucleation [1]. Thus, more nuclei can be formed on the side from which the CO_2 diffuses in because this region contains more CO_2. However, more nucleation points are accompanied by smaller pore sizes [35], originating from a competition between pore growth and nucleation [37]. Large pores are formed in sections with lower CO_2 concentration, as the supersaturation is lower and fewer nucleation points develop. Consequently, fewer nuclei are formed in the transition zone and only the CO_2 in proximity to these contributes to their growth. In the non-porous region, that is, close to the mold side, the CO_2 concentration is too low for the formation of nuclei, and no pores are observed.

Figure 4 displays the distance dependence of pore radius and density for samples processed at 60°C and 80°C. Here, zero depth corresponds to the wire mesh side of the sheet from where the diffusion took place. As expected, the average pore radius increases with increasing distance from the surface of facilitated diffusion. This gradual change in pore size along the thickness direction depends mainly on the process temperature. Interestingly, it is also influenced by the respective strength of the magnets. For lower magnet strengths, the maximal pore radii are observed in a deeper region of the polymer. This outcome indicates that the magnet strength influences the CO_2. The pressure exerted by the magnets might hinder the swelling of the polymer as it absorbs $scCO_2$ during the exposure time. This aspect could be further clarified with an autoclave equipped with an observation window, allowing the direct observation of the propagation of the diffusion front [29, 32].

3.3 | Characterization of the Imprinted Topography by AFM

To evaluate the successful transfer of the nano- and microstructures into the polymeric surface, we characterized the surface topography by AFM measurements. Figure 5 displays typical surface height maps of the applied molds and representative micro- and nanostructured samples. A comparison confirms that the structure of the molds is well replicated in the PMMA sheet. To analyze the influence of the foaming parameters on replication quality, we compare the height (from peak to valley) of the respective molds and structured sheets produced at different foaming temperatures, with different nominal magnet strengths and for different diffusion configurations (with and without mesh). All data points shown in Figure 6 are averages from multiple measurements at 2–3 different locations on each sample. No obvious trend was observed in terms of the considered foaming parameters. The average heights achieved for the micro-structured replicas are about 2.2 µm, and they correspond well to the structure height of the mold of about 2.4 µm. The nanostructured replicas have a height of about 260 nm which is again close to the mold height of about 312 nm.

It is important to mention that the imprinted heights can be influenced by factors other than the process parameters. For example, the detachment of the mold from the sample is a critical

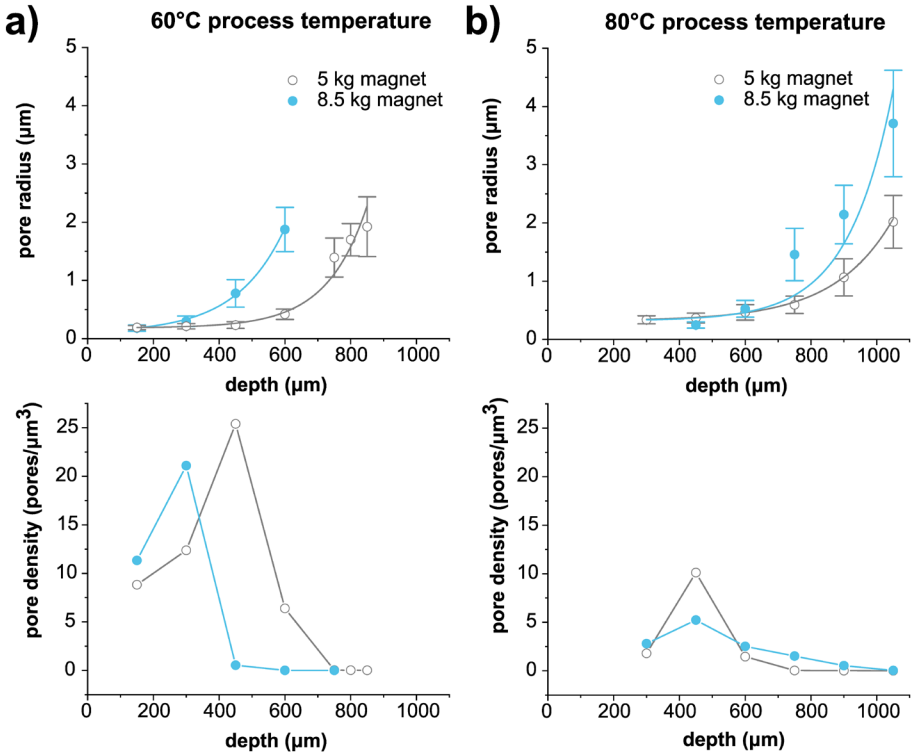

FIGURE 4 | Comparison of the average pore radius and density of PMMA sheets foamed at (a) 60°C and (b) 80°C with the two different magnet types (5 and 8.5 kg). The whiskers of the pore radii symbols indicate the standard deviation of the average. All lines are only guides to the eye. [Color figure can be viewed at wileyonlinelibrary.com]

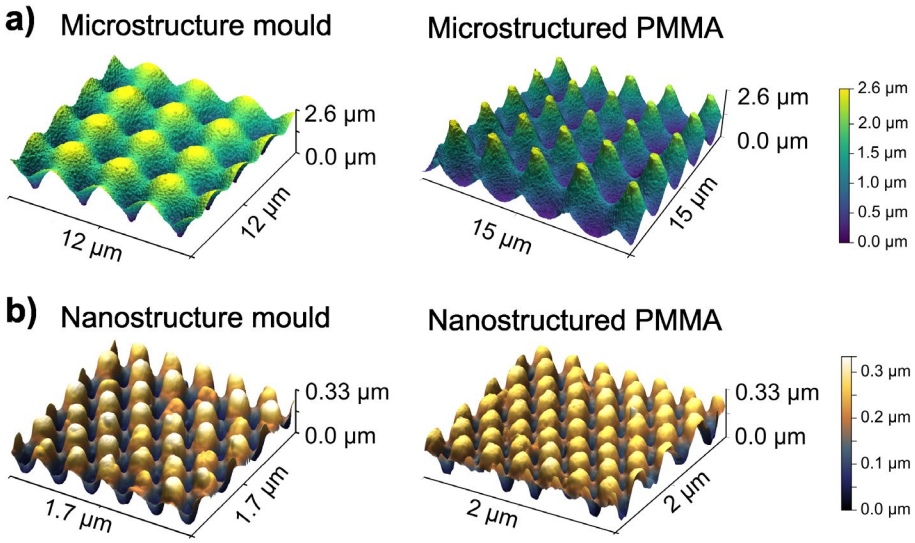

FIGURE 5 | Surface height maps recorded by AFM on the utilized molds with (a) micro- and (b) nanostructure resembling the bio-inspired surfaces of a lotus leave and a moth eye, respectively. The surface height maps of the positive replica on the right are shown for representative PMMA samples with micro- and nanostructured surface. Both samples were foamed at 60°C, clamped between two magnets of 8.5 kg nominal strength in the diffusion facilitating configuration with wire mesh, resulting in a foamed, white sheet of PMMA. [Color figure can be viewed at wileyonlinelibrary.com]

point at which the structures could be inadvertently deformed. Furthermore, there is swelling and subsequent shrinkage of the polymer during the foaming. Absorption of $scCO_2$ makes the polymer deformable; however, at the same time, it swells. Thus, it is pressed into the mold in a swollen state, but after the pressure drop, the CO_2 is released to the surrounding, and the polymer shrinks again.

Nonetheless, the height comparison indicates that also the difference in the pressure applied by the two magnets of different

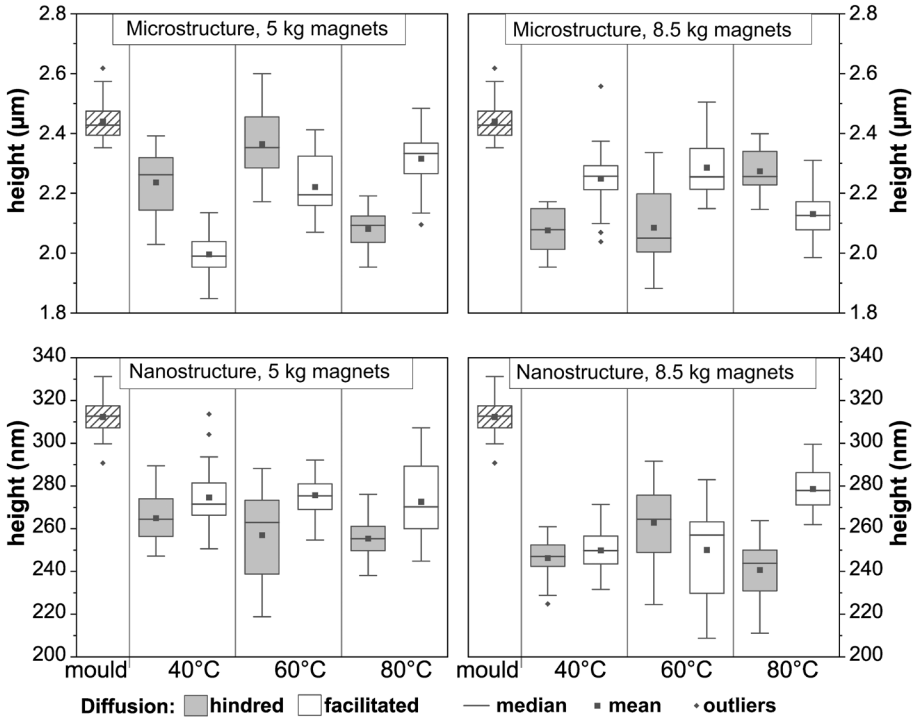

FIGURE 6 | Comparison of the obtained heights of the micro- and nanostructured samples processed at 40°C, 60°C, and 80°C processing temperature without and with the mesh facilitating CO_2 diffusion. Magnets with a nominal magnet strength of 5 and 8.5 kg were utilized. The height of the respective sample and the utilized molds were determined by multiple profile measurements at three points on each sample.

strength has no significant influence on the height of the replica structures, neither for the micro- nor for the nanostructure. We, therefore, speculate that it is possible that much lower contact pressures are sufficient for structuring (but not for effective foaming of white polymers). This assumption agrees with the results of Wang et al. [12] who used a weight of only 200 g for the imprinting of micro- and nanostructures into PMMA, even at comparable low temperature of 35°C and pressures of 4 to 19 MPa. However, as discussed in the previous subsection, the magnet strength influences pore size and density distribution.

3.4 | Surface Functionality: Contact Angles and Optical Reflection

After successful imprinting of the nano- and microstructures, a noticeable change in terms of surface functionalization can be expected. The microstructured mold is intended to increase the water repellence as it is inspired by a lotus leaf while the nanostructured mold is designed in accordance with a moth eye structure reducing optical reflection. Therefore, we measured both properties on the structured PMMA sheets.

First, we conducted contact angle measurements on different spots of the structured samples. A non-processed, flat PMMA sample served as reference. Figure 7 compares the average static contact angles for micro- and nanostructured samples processed at foaming temperatures of 40°C, 60°C, and 80°C, utilizing the 5 and 8.5 kg magnets. Both types of diffusion management (facilitated or hindered) were included in the assessment. Compared to the unstructured reference, the contact angle increased significantly due to the structuring. With an average contact angle of around 80°, the smooth, unprocessed PMMA surface is hydrophilic, but it becomes hydrophobic after structuring. The averaged contact angles measured on the structured sheets vary roughly between 110° and 120°, the whiskers represent the measured maximum and minimum values.

This outcome agrees with previous studies showing that introducing surface roughness enhances the contact angle of an initially flat PMMA surface [38, 39]. Our results are comparable to the study of Fritz et al. [38] who achieved static contact angles of $(121.0 \pm 6.0)°$ on patterned PMMA, although the flat PMMA exhibited a contact angle of $(72.2 \pm 2.0)°$. An even greater increase in the surface angle was reported by Ma et al. [39] who achieved superhydrophobic surfaces $(154.3 \pm 3.9)°$ from hydrophilic PMMA by a combination of micro- to nanoscale surface porosity and the reorientation of the hydrophobic and hydrophilic groups in the polymer chains.

In addition to the wetting behavior, a surface structure also influences optical properties. As previously mentioned, the nanostructured mold is designed to reduce the surface reflection in accordance with the moth eye effect [40, 41]. And, indeed, as shown in Figure 8a, the total reflectance of light is greatly reduced from about 10% for a flat reference sample to about 7% for transparent samples (hindered diffusion). The low reflectance for all samples observable for the short wavelength below 350 nm can be readily explained by the absorbing properties of PMMA in the UV [42].

However, also the inner structure of a material influences its optical appearance. As previously shown in Figure 2, the foaming

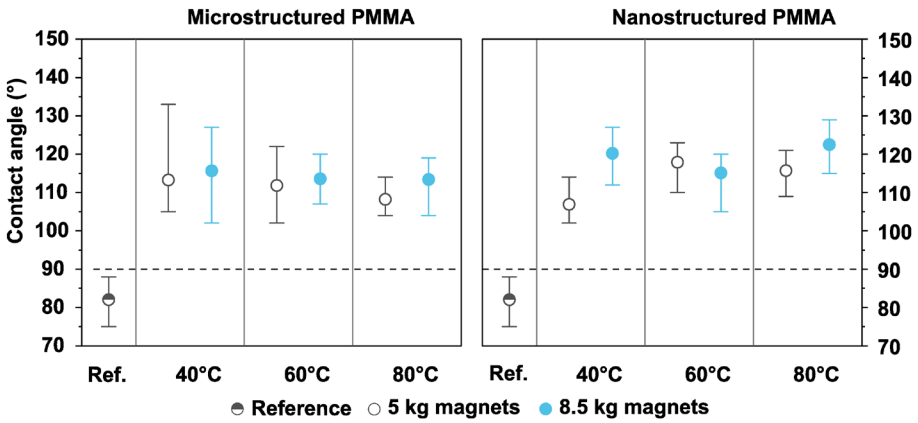

FIGURE 7 | Average static contact angles of micro- and nanostructured samples and a flat sheet of PMMA as reference. The structured samples were processed at 40°C, 60°C and 80°C foaming temperature for two different magnet strengths (5 and 8.5 kg). The whiskers indicate the maximum and minimum static contact angles achieved. The dashed line marks the border between hydrophilic (< 90°) and hydrophobic (> 90°) contact angles. [Color figure can be viewed at wileyonlinelibrary.com]

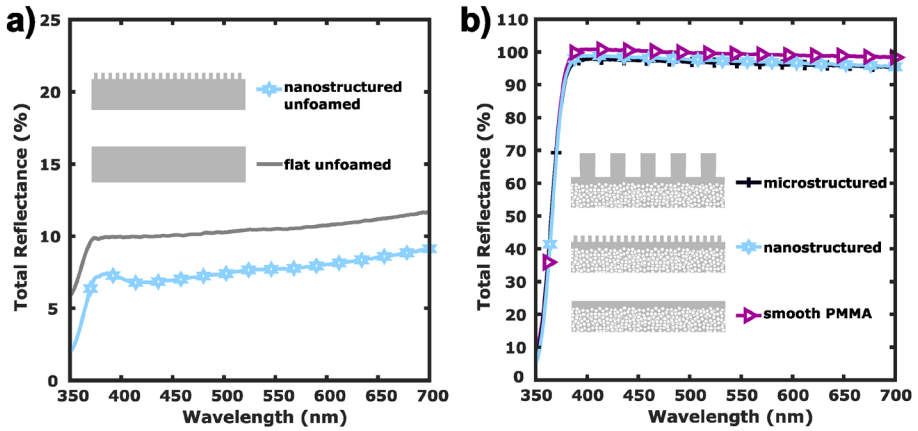

FIGURE 8 | (a) Total reflectance spectra of a transparent, nanostructured sample in comparison with a flat unfoamed PMMA sheet. The overall reflection is reduced on the nanostructured sample due to the moth eye effect. (b) Comparison of foamed, white PMMA samples imprinted with micro- and nanostructures and a flat, featureless surface. The reflection reducing effect of the nanostructure does not noticeably impair the reflectance for these highly scattering white samples. All samples were processed at 60°C with a nominal magnet strength of 5 kg. Each reflectance spectrum is averaged from three measurements. [Color figure can be viewed at wileyonlinelibrary.com]

with facilitated diffusion in wire mesh configuration turned all samples white. To determine their optical properties, we performed reflectance measurements for these, too. As already described, the foaming temperature influences the pore size and the layer thickness of the foamed part in the sample. At 40°C foaming temperature, the pores were about 100 nm in diameter, and the reflectance was consistently lower than for the samples foamed at 60°C or 80°C. These latter two did not differ significantly in reflectance, so that the samples foamed at 60°C are displayed in Figure 8b to emphasize the influence of the surface structure. Also, the different magnet types had negligible influence on the reflectance properties. Therefore, only the results for the 5 kg magnets are shown here (see Ref. [43] for more details and spectra).

As shown in Figure 8b, the micro- and nanostructured samples feature similar reflectance. They are even close to a smooth reference sample, foamed with a glass slide instead of a mold. The similar reflectance values achieved suggest that the surface structuring does not interfere with the high reflectance caused by the inner foam structure. Indeed, the reflectance is close to 100% in the visible range. This means that the foamed samples scatter nearly as well as the white reference standard due to the light scattering pores.

To conclude, we enhanced the static contact angle strongly for both types of imprinted surface structures, resulting in hydrophobic, but not superhydrophobic surfaces. Thus, water drops dispensed on the structures cannot roll off at low tilting angles, which is a prerequisite for self-cleaning inspired by plant leaves [44]. Nonetheless, the moth eye inspired nanostructure greatly reduces the surface reflection.

4 | Conclusion and Outlook

In this study, we demonstrated simultaneous molding and foaming of polymers utilizing supercritical carbon dioxide. The presented setup, where the mold is pressed into the polymer sheets

through two opposing magnets, can be easily integrated into an autoclave batch process. The micro- and nanostructures selected were inspired by biological structures, known from lotus leaves and insect compound eyes. Simultaneous foaming and structuring were achieved by an incomplete saturation of the polymer, whereby $scCO_2$ penetrates the side opposed to the mold, equipped with a wire mesh for facilitated diffusion. Although we applied the process to polymer sheets with a thickness of 1 mm, we expect that the thickness of the polymer sheets can be significantly thinner (a few hundreds of μm) or thicker (some mm) depending on the overall lateral size of the sheets (or foils) and the strength of the magnets. In any case, the actual process parameters like temperature, pressure, and saturation time depend on the utilized experimental set-up and the material properties of the respective polymer sample.

Thereby, foamed white polymers with imprinted structures in the micro- and nanometer range could be produced. A high reflectance over the entire visible spectrum was obtained. The height profiles of the molded structures were evaluated by AFM. The combination of foaming and structuring led to no adverse effect compared to exclusively patterned, transparent samples without an inner porous layer. The reduced wettability due to structuring was evaluated by contact angle measurements. The initially hydrophilic PMMA became hydrophobic for both structures, with static contact angles up to about 130°. The pore size and its gradient caused by the one-sided incomplete saturation were investigated by SEM.

For higher material efficiency, the method presented could also be applied to thinner polymer layers, whereby a shorter exposure time must be considered. A step towards self-cleaning could be imprinting microstructures superimposed with nanoscale features and the utilization of hydrophobic base materials. In addition, many other structure-based surface functionalizations could be of interest. This includes cicada wings covered with nanoscale pillars similar to moth-eye structures, which were found to kill bacteria based on the surface structure [45, 46], providing an appealing approach for antibacterial surfaces. Supercritical CO_2 assisted embossing could be interesting for such surfaces, in particular for microbial growth studies, as bothersome surface contamination with solvent residues, release agents or oxidized material is omitted [16].

Author Contributions

Luisa Maren Borgmann: conceptualization (lead), data curation (equal), formal analysis (equal), investigation (supporting), methodology (lead), project administration (lead), validation (equal), visualization (equal), writing – original draft (equal). **Ester Priante:** data curation (equal), formal analysis (equal), investigation (equal), writing – review and editing (supporting). **Siegbert Johnsen:** resources (equal), writing – review and editing (supporting). **Marc Schneider:** resources (equal), writing – review and editing (equal). **Markus Guttmann:** investigation (equal), resources (equal), writing – review and editing (equal). **Benedikt Bläsi:** resources (equal), writing – review and editing (equal). **Gabriele Wiegand:** resources (equal), writing – review and editing (equal). **Hendrik Hölscher:** conceptualization (equal), data curation (equal), methodology (equal), project administration (equal), resources (equal), supervision (lead), validation (equal), visualization (equal), writing – original draft (equal), writing – review and editing (lead).

Acknowledgments

It is a pleasure to thank our colleagues from the Institute of Microstructure Technology (IMT) and the Institute of Catalysis Research and Technology (IKFT) for their continuous support and help in the lab. This study was financially supported through the 'PROPOLIS' project funded by the Deutsche Forschungsgemeinschaft (DFG) through program DFG-SPP 1839 'Tailored disorder' (HO 2237/121). We also acknowledge support of the Karlsruhe Nano Micro Facility (KNMF, www.knmf.edu/knmf), a Helmholtz Research Infrastructure at Karlsruhe Institute of Technology (KIT, www.kit.edu). Open Access funding enabled and organized by Projekt DEAL.

Funding

This work was supported by Deutsche Forschungsgemeinschaft, HO 2237/121; Karlsruhe Nano Micro Facility (KNMFi).

Conflicts of Interest

The authors declare no conflicts of interest.

Data Availability Statement

Data available on request from the authors.

References

1. D. L. Tomasko, H. B. Li, D. H. Liu, et al., "A Review of CO_2 Applications in the Processing of Polymers," *Industrial & Engineering Chemistry Research* 42, no. 25 (2003): 6431–6456, https://doi.org/10.1021/ie030199z.

2. S. P. Nalawade, F. Picchioni, and L. P. B. M. Janssen, "Supercritical Carbon Dioxide as a Green Solvent for Processing Polymer Melts: Processing Aspects and Applications," *Progress in Polymer Science* 31, no. 1 (2006): 19–43, https://doi.org/10.1016/j.progpolymsci.2005.08.002.

3. L. J. M. Jacobs, M. F. Kemmere, and J. T. F. Keurentjes, "Sustainable Polymer Foaming Using High Pressure Carbon Dioxide: A Review on Fundamentals, Processes and Applications," *Green Chemistry* 10, no. 7 (2008): 731, https://doi.org/10.1039/b801895b.

4. S. L. Wells and J. DeSimone, "CO_2 Technology Platform: An Important Tool for Environmental Problem Solving," *Angewandte Chemie (International ed. in English)* 40 (2011): 518–527.

5. J. Syurik, R. H. Siddique, A. Dollmann, et al., "Bio-Inspired, Large Scale, Highly-Scattering Films for Nanoparticle-Alternative White Surfaces," *Scientific Reports* 7 (2017): 46637, https://doi.org/10.1038/srep46637.

6. L. Borgmann and H. Hölscher, "White Without TiO_2," *Kunststoffe International* (2020): 13–16.

7. L. M. Borgmann, S. Johnsen, C. Santos De Oliveira, et al., "Porous Polymeric Microparticles Foamed With Supercritical CO2 as Scattering White Pigments," *Bioinspiration & Biomimetics* 18, no. 2 (2023): 26011, https://doi.org/10.1088/1748-3190/acb899.

8. M. J. A. Ruszala, N. A. Rowson, L. M. Grover, and R. A. Choudhery, "Low Carbon Footprint TiO_2 Substitutes in Paint: A Review," *International Journal of Chemical Engineering and Applications* 6, no. 5 (2015): 331–340, https://doi.org/10.7763/ijcea.2015.V6.505.

9. M. D. Newman, M. Stotland, and J. I. Ellis, "The Safety of Nanosized Particles in Titanium Dioxide– And Zinc Oxide–Based Sunscreens," *Journal of the American Academy of Dermatology* 61, no. 4 (2009): 685–692, https://doi.org/10.1016/j.jaad.2009.02.051.

10. A. Weir, P. Westerhoff, L. Fabricius, K. Hristovski, and N. von Goetz, "Titanium Dioxide Nanoparticles in Food and Personal Care Products," *Environmental Science & Technology* 46, no. 4 (2012): 2242–2250, https://doi.org/10.1021/es204168d.

11. H. C. Winkler, T. Notter, U. Meyer, and H. Naegeli, "Critical Review of the Safety Assessment of Titanium Dioxide Additives in Food," *Journal of Nanobiotechnology* 16, no. 1 (2018): 51, https://doi.org/10.1186/s12951-018-0376-8.

12. Y. Wang, Z. Liu, B. Han, et al., "Compressed-CO_2-Assisted Patterning of Polymers," *Journal of Physical Chemistry B* 109, no. 25 (2005): 12376–12379, https://doi.org/10.1021/jp050954h.

13. S.-s. Nozaki and M. Ohshima, "A CO_2 Assisted Nanoimprinting and Cold Embossing," in *Proceedings of the 64th Annual Conference of the Society of Plastics Engineers (ANTEC 2006)* (ANTEC, 2006), 2551–2555.

14. W. M. Choi, M. Y. Song, and O. O. Park, "Compressed-Carbon Dioxide (CO_2) Assisted Nanoimprint Lithography Using Polymeric Mold," *Microelectronic Engineering* 83, no. 10 (2006): 1957–1960, https://doi.org/10.1016/j.mee.2006.02.003.

15. S. Y. Yang, T. C. Huang, J. K. Ciou, B. D. Chan, and J. G. Loeser, "CO_2-Assisted Embossing for the Fabrication of PMMA Components Under Low Temperature and With Low Pressure," *Journal of Micromechanics and Microengineering* 18, no. 2 (2008): 025024, https://doi.org/10.1088/0960-1317/18/2/025024.

16. S. Fujita, D. Ono, M. Ohshima, and H. Iwata, "Supercritical CO_2-Assisted Embossing for Studying Cell Behaviour on Microtextured Surfaces," *Biomaterials* 29, no. 34 (2008): 4494–4500, https://doi.org/10.1016/j.biomaterials.2008.08.027.

17. J. S. Chiou, J. W. Barlow, and D. R. Paul, "Plasticization of Glassy Polymers by CO_2," *Journal of Applied Polymer Science* 30, no. 6 (1985): 2633–2642, https://doi.org/10.1002/app.1985.070300626.

18. Y. T. Shieh, J. H. Su, G. Manivannan, et al., "Interaction of Supercritical Carbon Dioxide With Polymers. I. Crystalline Polymers," *Journal of Applied Polymer Science* 59, no. 4 (1996): 695–705, https://doi.org/10.1002/(SICI)1097-4628(19960124)59:4%3C695::AID-APP15%3E3.0.CO;2-P.

19. Y. T. Shieh, J. H. Su, G. Manivannan, et al., "Interaction of Supercritical Carbon Dioxide With Polymers. II. Amorphous Polymers," *Journal of Applied Polymer Science* 59, no. 4 (1996): 707–717, https://doi.org/10.1002/(SICI)1097-4628(19960124)59:4%3C707::AID-APP16%3E3.0.CO;2-M.

20. M. Worgull, *Hot Embossing - Theory and Technology of Micro Replication* (William Andrew, 2009).

21. C. Okolieocha, D. Raps, K. Subramaniam, and V. Altstadt, "Microcellular to Nanocellular Polymer Foams: Progress (2004–2015) and Future Directions - A Review," *European Polymer Journal* 73 (2015): 500–519, https://doi.org/10.1016/j.eurpolymj.2015.11.001.

22. S. K. Goel and E. J. Beckman, "Nucleation and Growth in Microcellular Materials: Supercritical CO_2 as Foaming Agent," *AICHE Journal* 41, no. 2 (1995): 357–367, https://doi.org/10.1002/aic.690410217.

23. Y. P. Handa and Z. Zhang, "A New Technique for Measuring Retrograde Vitrification in Polymer-Gas Systems and for Making Ultramicrocellular Foams From the Retrograde Phase," *Journal of Polymer Science Part B: Polymer Physics* 38, no. 5 (2000): 716–725, https://doi.org/10.1002/(SICI)1099-0488(20000301)38:5%3C716::AID-POLB9%3E3.0.CO;2-N.

24. A. V. Nawaby, Y. P. Handa, X. Liao, Y. Yoshitaka, and M. Tomohiro, "Polymer–CO_2 Systems Exhibiting Retrograde Behavior and Formation of Nanofoams," *Polymer International* 56, no. 1 (2007): 67–73, https://doi.org/10.1002/pi.2112.

25. D. C. Rodríguez, D. Carrascal, E. Solórzano, M. A. R. Pérez, and J. Pinto, "Analysis of the Retrograde Behavior in PMMA-CO2 Systems by Measuring the (Effective) Glass Transition Temperature Using Refractive Index Variations," *Journal of Supercritical Fluids* 170 (2021): 105159, https://doi.org/10.1016/j.supflu.2020.105159.

26. A. J. Wolf, H. Hauser, V. Kübler, C. Walk, O. Höhn, and B. Bläsi, "Origination of Nano- and Microstructures on Large Areas by Interference Lithography," *Microelectronic Engineering* 98 (2012): 293–296, https://doi.org/10.1016/j.mee.2012.05.018.

27. B. Bläsi, N. Tucher, O. Höhn, et al., "Large Area Patterning Using Interference and Nanoimprint Lithography," in *Proceedings of SPIE*, vol. 9888, ed. H. Thienpont, J. Mohr, H. Zappe, and H. Nakajima (SPIE, 2016), 98880H, https://doi.org/10.1117/12.2228458.

28. J. Schindelin, I. Arganda-Carreras, E. Frise, et al., "Fiji: An Open-Source Platform for Biological-Image Analysis," *Nature Methods* 9, no. 7 (2012): 676–682, https://doi.org/10.1038/nmeth.2019.

29. R. Li, N. Ye, V. Shaayegan, and T. Fang, "Experimental Measurement of CO_2 Diffusion in PMMA and Its Effect on Microcellular Foaming," *Journal of Supercritical Fluids* 135 (2018): 180–187, https://doi.org/10.1016/j.supflu.2018.01.024.

30. D. Nečas and P. Klapetek, "Gwyddion: An Open-Source Software for SPM Data Analysis," *Open Physics* 10, no. 1 (2012): 181–188, https://doi.org/10.2478/s11534-011-0096-2.

31. S. Orsi, E. Di Maio, S. Iannace, and P. A. Netti, "Hollow Micro- and Nano-Particles by Gas Foaming," *Nano Research* 7, no. 7 (2014): 1018–1026, https://doi.org/10.1007/s12274-014-0465-4.

32. L. N. Nikitin, E. E. Said-Galiyev, R. A. Vinokur, A. R. Khokhlov, M. O. Gallyamov, and K. Schaumburg, "Poly(Methyl Methacrylate) and Poly(Butyl Methacrylate) Swelling in Supercritical Carbon Dioxide," *Macromolecules* 35, no. 3 (2002): 934–940, https://doi.org/10.1021/ma010271+.

33. S. K. Goel and E. J. Beckman, "Generation of Microcellular Polymeric Foams Using Supercritical Carbon-Dioxide .1. Effect of Pressure and Temperature on Nucleation," *Polymer Engineering and Science* 34, no. 14 (1994): 1137–1147, https://doi.org/10.1002/pen.760341407.

34. J. Syurik, R. Schwaiger, P. Sudera, et al., "Bio-Inspired Micro-to-Nanoporous Polymers With Tunable Stiffness," *Beilstein Journal of Nanotechnology* 8 (2017): 906–914, https://doi.org/10.3762/bjnano.8.92.

35. C. Zhou, P. Wang, and W. Li, "Fabrication of Functionally Graded Porous Polymer via Supercritical CO_2 Foaming," *Composites Part B: Engineering* 42, no. 2 (2011): 318–325, https://doi.org/10.1016/j.compositesb.2010.11.001.

36. M. T. Ngo, J. S. Dickmann, J. C. Hassler, and E. Kiran, "A New Experimental System for Combinatorial Exploration of Foaming of Polymers in Carbon Dioxide: The Gradient Foaming of PMMA," *Journal of Supercritical Fluids* 109 (2016): 1–19, https://doi.org/10.1016/j.supflu.2015.09.030.

37. C. B. Park, D. F. Baldwin, and N. P. Suh, "Effect of the Pressure Drop Rate on Cell Nucleation in Continuous Processing of Microcellular Polymers," *Polymer Engineering & Science* 35, no. 5 (1995): 432–440, https://doi.org/10.1002/pen.760350509.

38. B. Fritz, M. Guttmann, P. C. Soler, et al., "Towards Mass Fabrication of Hot Embossed Plant Surface Texture Replicas as Photovoltaic Cover Layers," in *Nanoengineering: Fabrication, Properties, Optics, and Devices XV*, vol. 10730, ed. B. Panchapakesan, A. E. Sakdinawat, A. J. Attias, and E. A. Dobisz (SPIE, 2018), 107300J, https://doi.org/10.1117/12.2320555.

39. Y. Ma, X. Cao, X. Feng, Y. Ma, and H. Zou, "Fabrication of Super-Hydrophobic Film From PMMA With Intrinsic Water Contact Angle Below 90°," *Polymer* 48, no. 26 (2007): 7455–7460, https://doi.org/10.1016/j.polymer.2007.10.038.

40. P. B. Clapham and M. C. Hutley, "Reduction of Lens Reflexion by the 'Moth Eye's Principle'," *Nature* 244, no. 5 (1973): 281–282, https://doi.org/10.1038/244281a0.

41. D. G. Stavenga, S. Foletti, G. Palasantzas, and K. Arikawa, "Light on the Moth-Eye Corneal Nipple Array of Butterflies," *Proceedings of the*

Royal Society B 273, no. 1587 (2006): 661–667, https://doi.org/10.1098/rspb.2005.3369.

42. L. F. Nassier and M. H. Shinen, "Study of the Optical Properties of Poly (Methyl Methacrylate) (PMMA) by Using Spin Coating Method," *Materials Today: Proceedings* 60 (2022): 1660–1664, https://doi.org/10.1016/j.matpr.2021.12.213.

43. L. M. Borgmann, "Bio-Inspired White Porous Polymers Fabricated via Supercritical CO_2 Foaming," (PhD thesis, Karlsruhe Institute of Technology, 2023).

44. W. Barthlott, M. Mail, and C. Neinhuis, "Superhydrophobic Hierarchically Structured Surfaces in Biology: Evolution, Structural Principles and Biomimetic Applications," *Philosophical Transactions of the Royal Society A: Mathematical, Physical and Engineering Sciences* 374 (2016): 20160191, https://doi.org/10.1098/rsta.2016.0191.

45. E. P. Ivanova, J. Hasan, H. K. Webb, et al., "Natural Bactericidal Surfaces: Mechanical Rupture of *Pseudomonas aeruginosa* Cells by Cicada Wings," *Small* 8, no. 16 (2012): 2489–2494, https://doi.org/10.1002/smll.201200528.

46. S. Pogodin, J. Hasan, V. A. Baulin, et al., "Biophysical Model of Bacterial Cell Interactions With Nanopatterned Cicada Wing Surfaces," *Biophysical Journal* 104, no. 4 (2013): 835–840, https://doi.org/10.1016/j.bpj.2012.12.046.